

Hypervelocity impact damage prediction in composites: Part I—material model and characterisation

R.A. Clegg^{a,*}, D.M. White^a, W. Riedel^b, W. Harwick^b

^a*Century Dynamics Limited, Dynamics House, Hurst Road, Horsham, West Sussex RH12 2DT, UK*

^b*FhG—Ernst-Mach-Institut, Eckerstraße 4, D-79104 Freiburg, Germany*

Available online 16 November 2006

Abstract

This paper reports on the development of an extended orthotropic continuum material model and associated material characterisation techniques for the simulation and validation of impacts onto fibre reinforced composite materials. This part I of the paper focuses on the details of the numerical model and the material characterisation experiments. Part II (also in this volume) provides details of hypervelocity impact damage experiments and simulations performed to assess the capabilities of the developed model. Here a detailed description of the material model as implemented in AUTODYN is provided. The model is an extension of a previous effort that focused on allowing the correct thermodynamic response of orthotropic materials to be simulated under shock wave loading. Improved capabilities to allow prediction of the extent of damage and residual strength of fibre composite materials after impact are described along with a set of quasi-static and dynamic experiments used to characterise the directional non-linear strength and extent of damage. Application of the model and derived material data is demonstrated through the simulation of a hypervelocity impact event of an aluminium sphere impacting the Columbus module shielding system of the International Space Station.

© 2006 Published by Elsevier Ltd.

Keywords: Hypervelocity; Impact; Material model; Material characterisation; Kevlar

1. Introduction

The study of impacts on composite materials is a requirement for both manned and unmanned spacecraft structures. On manned spacecraft, such as the ISS, fibre reinforced composite materials are used in the primary shielding system used to mitigate the effects of orbital space debris impacts. On unmanned spacecraft carbon fibre reinforced composite materials are commonly employed for major structural components. Although such components are not designed to mitigate the effects of hypervelocity impact, the consequences in terms of secondary debris after such impacts is of concern in relation to the survivability of on-board equipment. This paper describes an advanced material model, and set of material characterisation experiments, for orthotropic materials. The accompanying paper [1] provides details of hypervelocity impact experiments and simulations performed to assess the capabilities of this model. The objective of this effort was

*Corresponding author. Tel.: +44 1403 270066; fax: +44 1403 270099.

E-mail address: richard.clegg@centurydynamics.co.uk (R.A. Clegg).

to improve the predictive capabilities of numerical simulations of hypervelocity impacts on a range of composite spacecraft structures/materials [2], such as those performed by AUTODYN [3].

The foundation for the material modelling and characterisation work presented here is described in detail in [4]. This work led to the identification of the following phenomena, which we believe are of primary interest for composite and textile materials subject to high/hypervelocity impact:

- material anisotropy
- shock response
- anisotropic strength degradation (damage).

The material model [2] developed to address these aspects of composite material simulation under impact loading is now described. The material model development was carried out “hand-in-hand” with material characterisation experiments which are also described alongside the model features.

2. Basic orthotropic stiffness and shock response

In anisotropic materials, the traditional independent approach for the solution of the equation of state and constitutive relations in a hydrocode is complicated because these two sub-models are strongly coupled; volumetric strain leads to deviatoric stress, and similarly deviatoric strain leads to spherical stress. A methodology [5] was implemented and further developed in AUTODYN as reported in [4]. Consider a linear elastic orthotropic material for which the total incremental stress, $\Delta\sigma_{ij}$, can be related to the total incremental strain, $\Delta\varepsilon_{ij}$, through the orthotropic stiffness matrix, C_{ij} . The coefficients of C_{ij} being functions of the orthotropic elastic material constants, E_{ii} , ν_{ij} and G_{ij} .

$$\Delta\sigma_{ij} = C_{ij} \left[\Delta\varepsilon_{ij}^d + \frac{1}{3} \Delta\varepsilon_v \right]. \quad (1)$$

To facilitate the coupling of the deviatoric and volumetric material response the total strain has been decomposed into volumetric, ε_v , and deviatoric, ε_{ij}^d , components. Since the pressure is the average of the three direct stresses, from Eq. (1) we can obtain

$$\begin{aligned} \Delta P = & -\frac{1}{9}(C_{11} + C_{22} + C_{33} + 2C_{12} + 2C_{23} + 2C_{31})\Delta\varepsilon_v \\ & -\frac{1}{3}(C_{11} + C_{21} + C_{31})\Delta\varepsilon_{11}^d - \frac{1}{3}(C_{12} + C_{22} + C_{32})\Delta\varepsilon_{22}^d - \frac{1}{3}(C_{13} + C_{23} + C_{33})\Delta\varepsilon_{33}^d. \end{aligned} \quad (2)$$

For an isotropic Hookean material the first term on the right-hand side of Eq. (2) is equivalent to a linear equation of state, whilst the remaining deviatoric strain terms would be zero. Thus for an orthotropic material we can replace the first term with a non-linear Mie–Grüneisen equation of state and the remaining terms act as a correction due to deviatoric strains.

A model based on the above was implemented in AUTODYN [3] and has subsequently been used for simulating high to hypervelocity impacts on a wide range of applications and materials [6–10]. This experience identified potential weaknesses of the model, especially with respect to anisotropic strength degradation. Characterising and modelling these aspects is the main focus of the current work.

The phases of anisotropic strength degradation in a composite material can be categorised into

- Nonlinear hardening (maximum stress increases with strain)
- Nonlinear softening (maximum stress decreases with strain)

The observed material characteristics, and tests to derive them, are now outlined along with the macro-mechanical material modelling features developed to represent the behaviour.

2.1. Non-linear hardening

Many composite materials exhibit non-linear stress strain behaviour when subject to tensile uniaxial stress loading. The most common example of such behaviour is found when loading a unidirectional fibre reinforced laminate at 45° to the fibre direction (Fig. 1). The observed non-linear response results in a reduction in the tangent material stiffness with strain.

The envelope to the stress strain curves (Fig. 1) clearly shows non-linear hardening behaviour. Cyclic unloading and re-loading also reveals that the non-linear hardening results in irreversible deformation. This terminology is consistent with that used for dislocation plasticity. However, in this case the underlying micro/meso-mechanical behaviour may include a number of different mechanisms such as matrix plasticity, fibre re-orientation and matrix/fibre damage. The baseline material model [4] employs a linear elastic orthotropic stiffness matrix under small tensile strains, hence it is not capable of capturing this type of behaviour.

To enable phenomenological representation of this hardening behaviour, a generalised limit surface [11] has been adopted. This surface is quadratic in stress space and is generally applicable to composite materials. For example, no a priori assumptions are made in respect of the influence of hydrostatic stress on inelastic deformation as in Hill's orthotropic yield criteria [12].

$$f = a_{11}\sigma_{11}^2 + a_{22}\sigma_{22}^2 + a_{33}\sigma_{33}^2 + 2a_{12}\sigma_{11}\sigma_{22} + 2a_{23}\sigma_{22}\sigma_{33} + 2a_{13}\sigma_{11}\sigma_{33} + 2a_{44}\sigma_{23}^2 + 2a_{55}\sigma_{31}^2 + 2a_{66}\sigma_{12}^2 - k \leq 0, \quad (3)$$

where the stresses σ_{ij} refer to the principal material directions, and k is a state variable defining the instantaneous value of the limit surface. The nine coefficients, a_{ij} define the extent of anisotropy in the material response and are constants, implying isotropic hardening. It can be shown [11] that these constants are related to the plastic Poisson ratio (PPR) in the material via

$$\begin{aligned} a_{11} &= a_{22} \frac{v_{21}^P}{v_{12}^P}, & a_{33} &= a_{22} \frac{v_{23}^P}{v_{32}^P}, & a_{11} &= a_{33} \frac{v_{31}^P}{v_{13}^P}, \\ a_{12} &= -a_{22} v_{21}^P, & a_{23} &= -a_{22} v_{23}^P, & a_{13} &= -a_{33} v_{31}^P. \end{aligned} \quad (4)$$

The values of the coefficients can thus be obtained from a series of well-instrumented tension and shear experiments. Fig. 2 shows the results of a typical in-plane and through thickness instrumented tension test on an aramid-fibre-epoxy specimen [2]. Note the non-linear characteristics of both the in-plane and out-of-plane Poisson ratio. For the purpose of the numerical model, this data must be linearised into an elastic and inelastic Poisson ratio.

In terms of numerical implementation, an iterative backward-Euler procedure [13] is used to return trial elastic stresses, which lie outside the limit surface, normally back to the limit surface. The associated incremental inelastic strains are defined using the Prandtl–Reuss equations, often called an associated flow

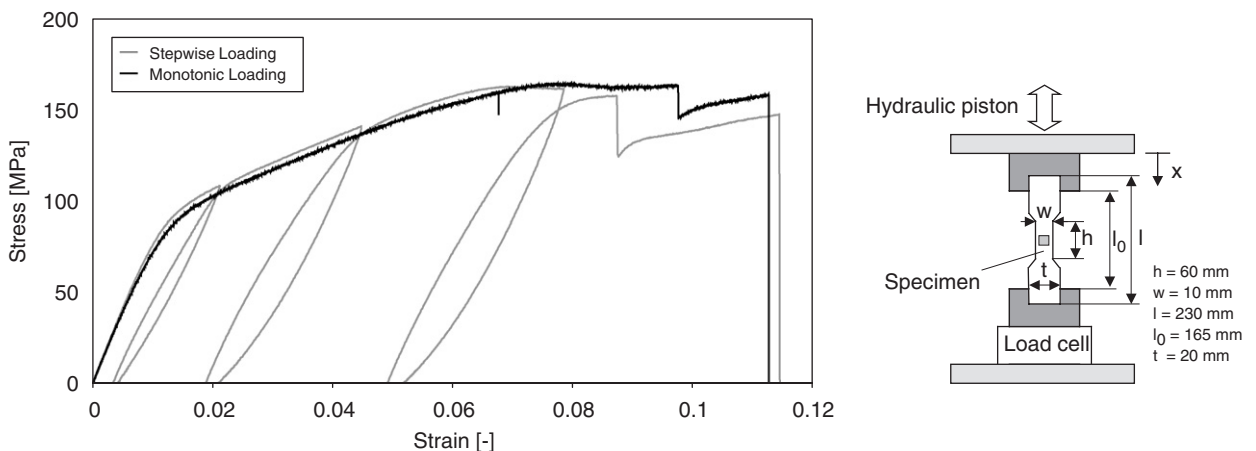


Fig. 1. Uniaxial tension test, cyclic stress strain curve for kevlar-epoxy ($0^\circ/90^\circ$) loaded at 45° to the fibre direction [2].

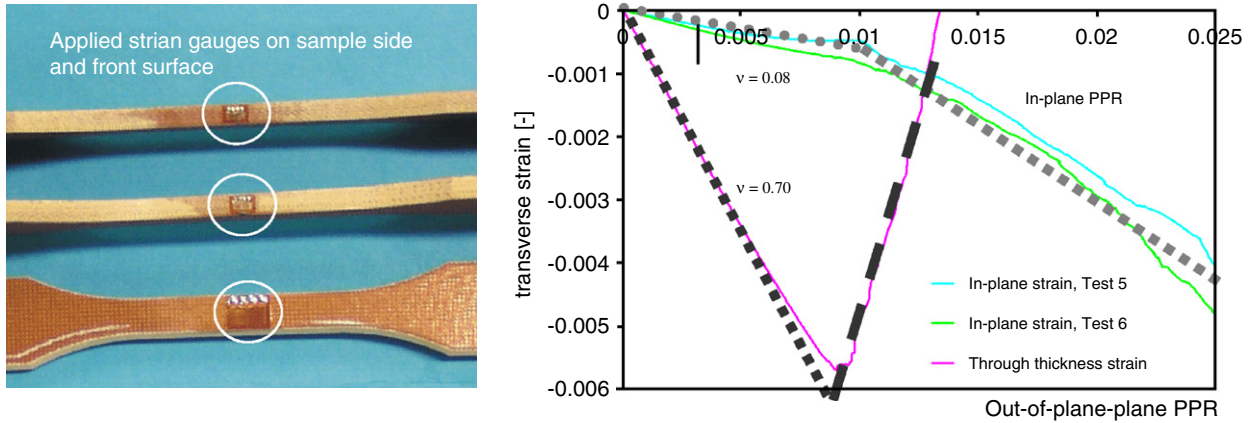


Fig. 2. Uniaxial tension test, measurement of elastic and plastic Poisson's ratio [2].

rule, and state that the plastic strain increments are proportional to the stress gradient of the yield function. The proportionality constant, $d\lambda$, is known as the plastic strain-rate multiplier. Written out explicitly the inelastic strain increments are given by

$$\begin{Bmatrix} d\epsilon_{11}^p \\ d\epsilon_{22}^p \\ d\epsilon_{33}^p \\ d\epsilon_{23}^p \\ d\epsilon_{31}^p \\ d\epsilon_{12}^p \end{Bmatrix} = \begin{Bmatrix} 2a_{11}\sigma_{11} + 2a_{12}\sigma_{22} + 2a_{13}\sigma_{33} \\ 2a_{12}\sigma_{11} + 2a_{22}\sigma_{22} + 2a_{23}\sigma_{33} \\ 2a_{13}\sigma_{11} + 2a_{23}\sigma_{22} + 2a_{33}\sigma_{33} \\ 4a_{44}\sigma_{23} \\ 4a_{55}\sigma_{31} \\ 4a_{66}\sigma_{12} \end{Bmatrix} d\lambda, \tag{5}$$

from which an equivalent inelastic strain measure can be derived [2] to yield

$$(d\epsilon^p)^2 = \frac{8}{3} f d\lambda^2. \tag{6}$$

This in turn feeds back into the hardening function, k , of the limit surface.

The developed non-linear hardening option, in combination with the baseline model, allows for much improved simulation of the non-linear in-plane hardening behaviour of fibre composite materials as shown in Fig. 3.

2.2. Non-linear softening (damage)

Considering failure in fibre composite materials, delamination caused by through thickness strain, shear strain causing matrix cracking, and fibre failure are the dominant modes of damage for impact loading. These modes of failure lead to a reduction in load carrying capacity in one or more material directions—we shall term this phase of deformation as softening (reduction in capability to hold stress with strain). A key characteristic here is the anisotropic nature of the effects of failure on the residual strength of the material. For example delamination leaves the material with zero tensile strength across the fibres, but significant tensile strength remains in the plane of the fibres.

To understand and quantify this type of phenomena a range of material characterisation tests must be performed to establish; the point at which softening starts to occur, the rate at which the material softens to zero strength in a particular material direction. These features determine the energy absorbed during the damage process.

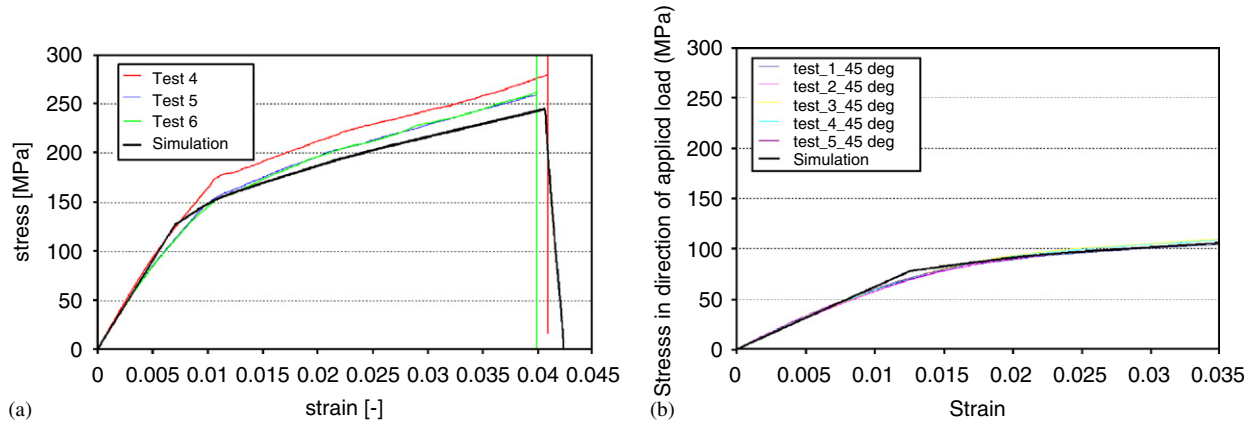


Fig. 3. Aramid-fibre-epoxy uniaxial stress tension tests—experiment and simulation. (a) Loading at 0° to fibre direction; (b) Loading at 45° to fibre direction.

The modelling approach taken here introduces additional failure initiation criteria and associated limit surfaces in material stress space, to represent specific modes of failure. Modified forms of the well-known Hashin failure criteria [14] have been adopted for both the failure initiation criteria and additional limit surfaces.

$$ii\text{-plane} :: e_{iif}^2 = \left(\frac{\sigma_{ii}}{\sigma_{ii,\text{fail}}(1 - D_{ii})} \right)^2 + \left(\frac{\sigma_{ij}}{\sigma_{ij,\text{fail}}(1 - D_{ij})} \right)^2 + \left(\frac{\sigma_{ik}}{\sigma_{ik,\text{fail}}(1 - D_{ik})} \right)^2 \geq 1. \quad (7)$$

The above failure initiation criteria are checked at each material integration point each cycle. If one of the failure criteria is exceeded ($e_{iif} > 1$), the orthotropic damage model is activated for that integration point. The damage model has several aspects.

2.2.1. An updated elastic material stiffness matrix

$$C_{ij} = \begin{pmatrix} C_{11} & C_{12}(1 - \text{Max}(D_{11}, D_{22})) & C_{13}(1 - \text{Max}(D_{11}, D_{33})) & 0 & 0 & 0 \\ C_{12}(1 - \text{Max}(D_{11}, D_{22})) & C_{22} & C_{23}(1 - \text{Max}(D_{22}, D_{33})) & 0 & 0 & 0 \\ C_{13}(1 - \text{Max}(D_{11}, D_{33})) & C_{23}(1 - \text{Max}(D_{22}, D_{33})) & C_{33} & 0 & 0 & 0 \\ 0 & 0 & 0 & C_{44} & 0 & 0 \\ 0 & 0 & 0 & 0 & C_{55} & 0 \\ 0 & 0 & 0 & 0 & 0 & C_{66} \end{pmatrix}. \quad (8)$$

2.2.2. Limit surfaces in material stress space and damage law

Additional limit surfaces are defined in material stress space through the failure initiation criteria in each material plane. If a stress point lies outside a limit surface, it is associatively returned to the limit surface using an iterative backward-Euler procedure [13]. Returning a stress point to a softening limit surface results in inelastic crack strain.

The resulting inelastic strain $\epsilon_{ij}^{\text{cr}}$ is then used as input to an *orthotropic damage evolution law*

$$D_{ij} = \left(\frac{L_{ij} F_{ij}^2}{2G_{ij}^f} \right) \left(\frac{\epsilon_{ij}^{\text{cr}}}{F_{ij}} \right), \quad (9)$$

where F_{ij} represents the initial failure stress in the three material directions and shear, G_{ij}^f is the fracture energy for each mode of failure and L_{ij} a local characteristic dimension of the numerical integration point in each

direction. This damage equation is formulated such that the work required to extend a crack by a unit length is relatively insensitive to the local element size in each direction and is an extension of the model developed for isotropic materials [15].

2.2.3. Damage characterisation

The material data requirement for the orthotropic softening model was purposely limited to the direct and shear failure initiation stress (F_{ij}) in each of the material planes, and the associated fracture energy release rates (G_{ij}^f) for mode I and II crack growth. A variety of material characterisation experiments were developed and used to populate the parameters of the failure surfaces.

Static damage characterisation tests

For the cross-woven aramid-fibre-epoxy laminate under consideration (Kevlar/129-epoxy), transverse isotropy was assumed. In this case the parameters for the failure surfaces in the two material planes perpendicular to the fibres could be derived from the in-plane uniaxial tension tests, as detailed above: The tensile failure initiation stress could be obtained directly from the experiment; the in-plane shear failure stress was derived through numerical simulation and calibration to match the experimental results for in-plane tension at 45° to the fibres (Fig. 3).

The transverse shear failure stress (mode II) was assumed to be equal to the inter-laminar shear failure stress and derived from a double notched shear test as described in Fig. 4(a) (performed according to standard proposal ASTM D 3846-79 and optimised according to Ref. [16] to compensate for normal stresses). The mode II delamination energy was derived using an end notch flexure test as described in Fig. 4(b) (performed in accordance with standard proposal EN 6034). A predefined crack propagates as a result of the specimen bending and associated shear forces at the crack tip in the Mode II loading. The total fracture energy G_{IIC} is calculated from the initial crack length, the critical load to start the crack and the associated piston displacement at the onset of crack propagation.

The through thickness (mode I) delamination energy was obtained using a double cantilever beam test arrangement as described in Fig. 4(c) (performed in accordance with the standard proposal EN6033). An initial delamination or pre-crack is introduced at the tip of the specimen with a diamond saw. The pre-cracked specimen is loaded continuously by the loading device until a total propagated crack length of 100 mm is achieved. The mode I fracture energy can be derived from the resulting load displacement curves.

A major challenge for the characterisation and modelling of fibre reinforced composites subject to impact is the through thickness (transverse shear) mode of deformation. Little attention is paid in the literature to this

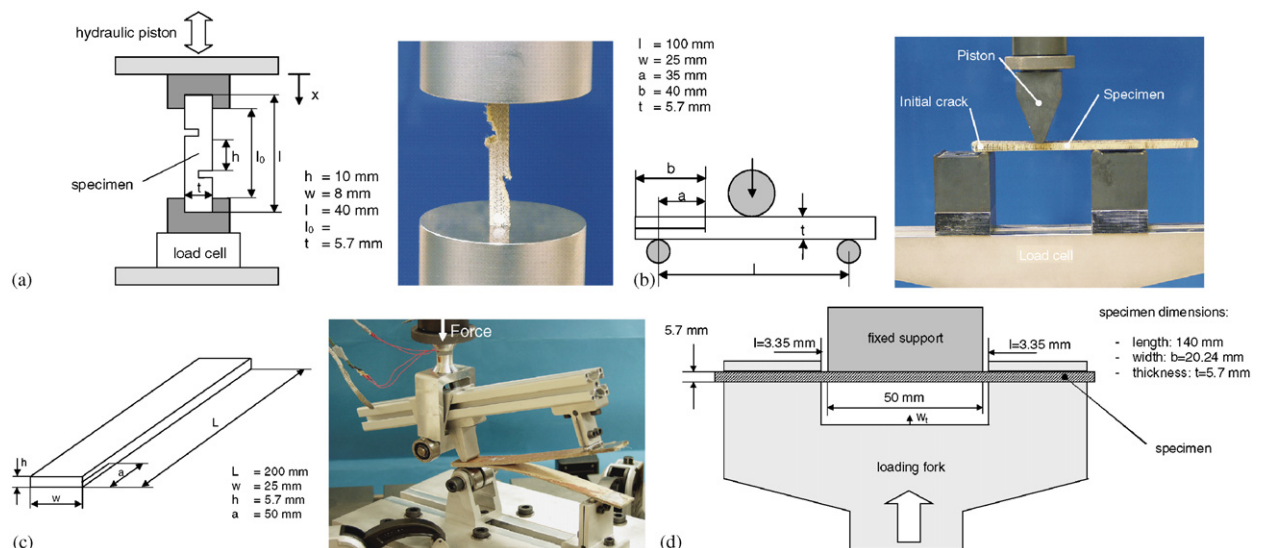


Fig. 4. (a) Double notched shear test; (b) end notched flexure test; (c) double cantilever beam test; (d) short beam bending test.

mode of deformation, most composite research being focussed on in-plane and bending response (structural behaviour). In this work a short beam bending test [2] was used to try to characterise the through thickness behaviour (Fig. 4(d)).

Dynamic damage characterisation tests

Planar plate impact tests were used here to estimate the spall strength (through thickness tensile strength) of the material. The tests consisted of a 3 mm thick aluminium alloy flyer impacting 5.65 mm thick aramid-fibre–epoxy laminate at velocities between 100 and 255 m/s. A laser interferometer was used to measure the particle velocity on the rear surface of the target.

To derive the through thickness tensile strength at high strain rates a superposition of release waves is generated in the target plate. Therefore the ratios of plate thicknesses and shock velocities are adapted to superimpose release waves from the target free surface and from the projectile rear side in the sample (target) material. Fig. 6 shows the velocity signals recorded at the target free surface of the aramid-fibre–epoxy composite. Note that in comparing experiment with numerical simulations of the configurations using accurate shock data for the material [4], mismatches are observed with respect to rise time and the shock plateau level. So far, shock dispersion in the composite sample is assumed to be the reason for this unexpected experimental behaviour. Although spallation measurements with the aramid-fibre–epoxy composite are not as successful as for metals, estimates for input to the material model could be obtained.

2.3. Final material model, data and required material characterisation

The full set of capabilities of the developed model for fibre composite materials can be summarised:

- Orthotropic elastic stiffness
- Non-linear and energy dependent volumetric response for high compressions
- Non-linear orthotropic strength with isotropic hardening
- Stress based failure initiation on each material plane
- Orthotropic damage based on fracture energy

The required input parameters and the matrix of material characterisation tests used to derive each parameter is presented in Table 1. Data derived for the aramid-fibre–epoxy laminate considered here is also provided.

3. Validation

Initial validation and assessment of the developed material model and derived input was performed using dynamic planar plate impact experiments [2]. Here we shall discuss two examples of this type of test. Further examples are described in part II of the paper [1] along with hypervelocity impact validation.

3.1. Inverse plate impact

During development of the baseline model [4] inverse plate impact experiments were reported from which the uniaxial compression behaviour at strain rates up to 10^4 /s was studied for aramid-fibre–epoxy composites. In these sets of experiments a 50 mm diameter projectile composed of aramid-fibre–epoxy with a C45-steel backing plate impacts a stationary witness plate also made of C45-steel. A VISAR laser interferometer system recorded the velocity trace of the witness plate during the impact. Simulations of these experiments are repeated here using the enhanced material model and data to ensure that the addition of the non-linear strength and damage aspects of the model did not prejudice the models ability to reproduce the transient shock wave propagation phenomena. The simulations were performed using the Lagrange solver of AUTODYN [3] in a uniaxial strain configuration with element size of 0.1 mm. Fig. 5 demonstrates the ability of the model to reproduce experimental VISAR signals at three velocities.

Table 1
Model input data and derived material constants for Kevlar epoxy

Equation of state: orthotropic		Strength model: orthotropic yield (non-linear hardening)	
Parameter	Source	Parameter	Source
$\rho = 1.65000\text{E}+00 \text{ g/cm}^3$	Direct measurement	$a_{11} = 1.50000\text{E}+00$	0° tension test
$E_{11} = 1.94800\text{E}+06 \text{ kPa}$	Uniaxial tension tests	$a_{22} = 1.00000\text{E}+00$	0° tension test
$E_{22} = 1.79898\text{E}+07 \text{ kPa}$	0° tension test	$a_{33} = 1.00000\text{E}+00$	0° tension test
$E_{33} = 1.79898\text{E}+07 \text{ kPa}$	0° tension test	$a_{12} = -6.80000\text{E}-01$	0° tension test
$\nu_{12} = 7.56000\text{E}-02$	0° tension test	$a_{13} = -6.80000\text{E}-01$	0° tension test
$\nu_{23} = 7.56000\text{E}-02$	0° tension test	$a_{23} = -2.60000\text{E}-01$	0° tension test
$\nu_{31} = 6.98000\text{E}-01$	Confined compression test [4]	$a_{44} = a_{55} = a_{66} = 4.00000\text{E}+00$	45° tension test
$G_{12} = 2.23500\text{E}+05 \text{ kPa}$	45° tension test	Plastic strain = 0.0, 9.0E-6, 6.2E-4, 1.9E-3, 2.5E-3, 5.0E-3, 8.8E-3, 1.2E-2, 2.6E-2	0° tension test
$G_{23} = 1.85701\text{E}+06 \text{ kPa}$	Short beam shear test	Effective stress = 1.55E5, 1.55E5, 1.67E5, 1.78E5, 1.87E5, 1.93E5, 2.10E5, 2.35E5, 2.52E5, 3.16E5 kPa	0° tension test
$G_{31} = 2.23500\text{E}+05 \text{ kPa}$	Short beam shear test		
$T_{\text{ref}} = 3.00000\text{E}+02 \text{ K}$	—		
$C_v = 1.42000\text{E}+03 \text{ J/kgK}$	Literature		
Sub-equation of state: polynomial		Failure model: orthotropic damage (non-linear softening)	
$A_1 = 5.89499\text{E}+06 \text{ kPa}$	Planar plate impact tests	$\sigma_{\text{fail}11} = 4.50000\text{E}+04 \text{ kPa}$	Calibration to match PPI spall and DCB tests
$\sigma_{\text{fail}22} = 2.45000\text{E}+05 \text{ kPa}$	Planar plate impact tests	$\sigma_{\text{fail}33} = 2.45000\text{E}+05 \text{ kPa}$	0° tension test
$A_2 = 5.00000\text{E}+07 \text{ kPa}$	Planar plate impact tests	$\sigma_{\text{fail}12} = 1.40000\text{E}+04 \text{ kPa}$	Interlamina shear test
$T_1 = 5.89500\text{E}+06 \text{ kPa}$	Assumed equal to A1	$\sigma_{\text{fail}23} = 2.00000\text{E}+04 \text{ kPa}$	Calibration to match 45° tension test
		$\sigma_{\text{fail}31} = 1.40000\text{E}+04 \text{ kPa}$	Interlamina shear test
		$G_f11 = 5.44710\text{E}+02 \text{ J/m}^2$	Double cantilever beam test
		$G_f 22 = 3.00000\text{E}+01 \text{ J/m}^2$	Calibrated to 0° tension test
		$G_f12 = G_f23 = G_f31 = 1.46130\text{E}+03 \text{ J/m}^2$	End notched flexure test

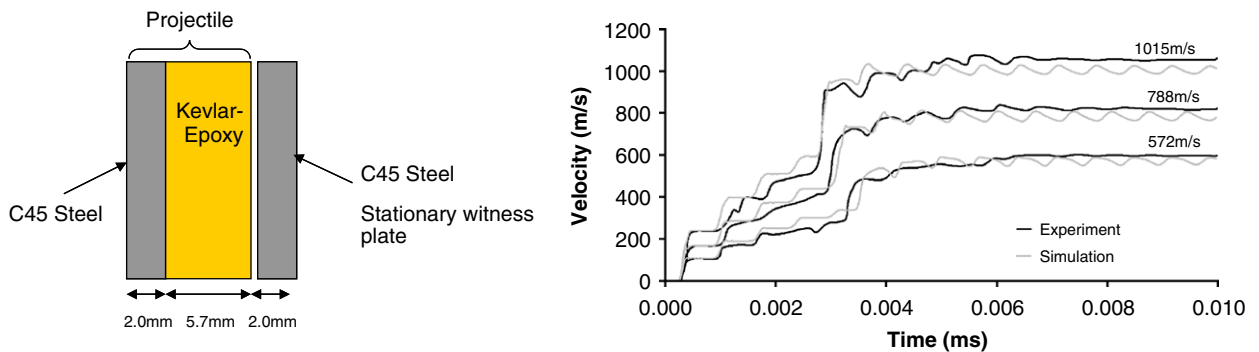


Fig. 5. Aramid-fibre-epoxy inverse flyer plate experiments and simulation comparisons (572, 788, 1055 m/s).

3.2. Plate impact damage

Both direct and symmetric planar plate impact tests were performed at different velocities to provide a basis for validating the ability of the numerical model to predict damage levels for given impact conditions [2]. 2D

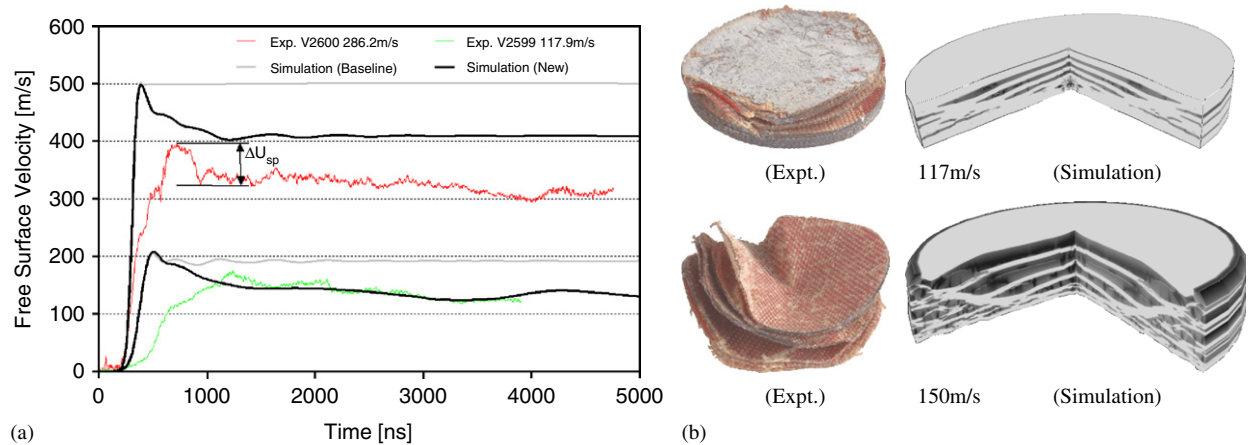


Fig. 6. Planar plate impact test. (a) Target rear surface velocity; (b) recovered samples and simulated delamination.

axisymmetric simulations of these tests were conducted using the Lagrange solver of AUTODYN [3] and the material model and data as described in [2]. Elements of side 0.1 mm were used throughout. The results are presented and compared with the experiment, and results using the baseline material model and data [4] (Fig. 6).

The key item to correlate between simulation and experiment is the magnitude of the pull-back spall signal observed in the tests. For the higher velocity, the experiment shows a pull-back spall signal of 62 m/s. The simulation with the original baseline model and data does not show any velocity reduction after the peak velocity. The new extended model and data gives a reduction of 58 m/s by release waves, which is similar to the observed signal.

The samples recovered from the experimental tests all showed extensive delamination, illustrating that the spall strength was exceeded in all tests. Contours of simulated through thickness damage are consistent with experimental observations (Fig. 6).

The results of simulations of a symmetric planar plate impact test with the enhanced model and data show a more marked improvement in the prediction levels of damage levels over the original base model. This configuration is further discussed in detail in part II [1].

4. HVI simulation—Columbus module shielding

Hypervelocity impact simulations on the Columbus shielding configuration using the baseline material model have previously been conducted and reported in [4]. These 2D axisymmetric simulations have been repeated here using the enhanced material model and data. Comparisons with the previous simulation work and experiments [2] are discussed. The case of a 15 mm diameter Al2007 sphere impacting the shielding configuration at 6500 m/s (Test case A8611, [4]), is described here.

The projectile, first bumper (aluminium) and the second bumper (Nextel and Kevlar-epoxy) are represented using the SPH solver with smoothing length of 0.25 mm. The rear wall is represented using the Lagrange solver with element edge size of 0.25 mm out to a radius of 60 mm. Gradual transition to larger elements is then made to a final radius of 200 mm for efficiency purposes.

Fig. 7 highlights the through thickness damage (delamination) predicted. It can be seen that during the impact extensive delamination/damage occurs in the immediate vicinity of the impact (Light grey regions Fig. 7). However the lateral growth in delamination is significantly less for the latest model and data. This correlates better with experimental observations compared with previous simulations [4]. As observed in experiment, the new simulation predicts cratering of the backwall with number. This represents a refined prediction of rear-wall damage over equivalent simulations performed using the baseline material model and data [4], as quantified in Table 2.

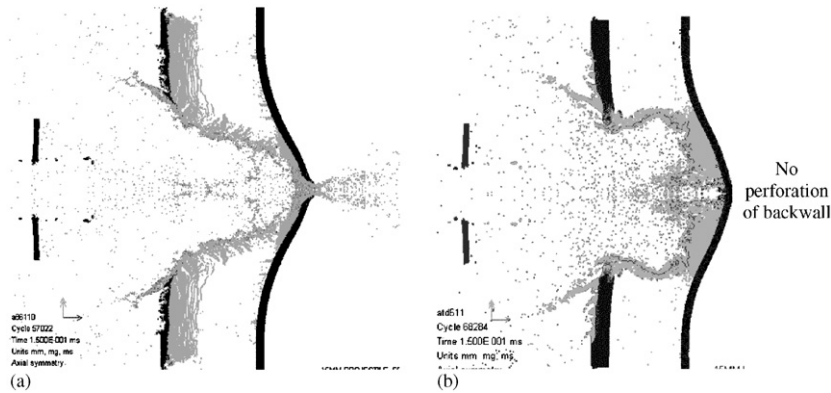


Fig. 7. 2D Axisymmetric simulation of Alenia/EMI test A8611 [2]: (a) final damage, old model and data [4]; (b) final damage, new model and data [4].

Table 2
Columbus shield HVI simulations, quantitative damage comparison

Test/ident	Bumper hole	Nextel hole	Kevlar/epoxy		Back wall		
			Front	Back	Hole	Crater	Pl. def.
Experiment	26.55	95	68	52	N/A	1.2	227.5
Original Simulation [4]	29	96	94	46	6	N/A	174
New simulation [2]	30	88	77	75	N/A	1.5	180

5. Conclusions

An improved continuum material model suitable for modelling impact on composite materials under low to hypervelocity impact conditions has been developed and implemented in AUTODYN [3]. The model is now capable of representing orthotropic elastic stiffness, non-linear shock effects, orthotropic non-linear hardening and orthotropic non-linear damage. The features of the model can be turned on/off as required for the material being simulated and the available input data. The model is designed to be applicable to a wide range of orthotropic materials under low to hypervelocity impact conditions.

An extensive experimental programme covering a wide range of static and dynamic tests was conducted “hand-in-hand” with the numerical modelling work. This included both material characterisation experiments for directional strength and failure, delamination energy and equation of state measurement. Additionally new impact experiment configurations were developed to allow quantitative assessment of the extent of damage development in composite materials under different loading conditions.

Throughout the model development and experimental programme, an extensive simulation programme was used to support the model development and assess and validate the improved composite material model. This included simulation of material characterisation tests to verify that the model could reproduce the underlying material response observed in experiments, simulation of impact damage experiments to assess the evolving material model and supplied input data, simulation of hypervelocity impact events on simplified and representative shielding configurations to assess the performance of the new model and data on the target application. Further application and validation of the final model and input data is described in part II of this paper [1].

Acknowledgements

This work was funded by ESA/ESTEC under Contract no. 12400/97/NL/PA(SC), CCN no. 2. The authors gratefully acknowledge the direction and advice provided by Michel Lambert of ESTEC.

References

- [1] Riedel W, Nahme H, White DM, Clegg RA. Hypervelocity impact damage Prediction in composites, part II—experimental investigation and simulations. *Int J Impact Eng*, this volume, 2005.
- [2] Riedel W, Harwick W, White DM, Clegg RA. Advanced material damage models for numerical simulation codes. Fhg-EMI report no. I 75/03, ESA CR(P) 4397, 2003.
- [3] Century Dynamics. AUTODYN theory manual. 2005.
- [4] Hiermaier SJ, Riedel W, Hayhurst CJ, Clegg RA, Wentzel CM. Advanced material models for hypervelocity impact simulations. EMI report no. E43/99, ESA CR(P) 4305, 1999.
- [5] Anderson CE, Cox PA, Johnson GR, Maudlin PJ. A constitutive formulation for anisotropic materials suitable for wave propagation computer program-II. *Comput Mech* 1994;15:201–23.
- [6] Hayhurst CJ, Livingstone IH, Clegg RA, Destefanis R, Faraud M. Ballistic limit evaluation of advanced shielding using numerical simulations. *Int J Impact Eng* 2001;26:309–20.
- [7] Clegg RA, Hayhurst CJ, Nahme H. Validation of an advanced material model for simulating the impact and shock response of composite materials. APS SCCM 2001.
- [8] White DM, Taylor EA, Clegg RA. Numerical simulation and experimental characterisation of direct hypervelocity impact on a spacecraft hybrid carbon fibre/kevlar composite structure. *Int J Impact Eng* 2003;29:779–90.
- [9] Silva MAG, Cismasiu C, Chiorean CG. Numerical simulation of ballistic impact on composite laminates. *Int J Impact Eng* in press, doi:10.1016/j.ijimpeng.2004.01.011.
- [10] Riedel W, Thoma K, et al. Vulnerability of composite aircraft components to fragmenting warheads—experimental analysis, material modeling, numerical studies. In: *Proceedings of the 20th international symposium on ballistics* 2002.
- [11] Chen JK, Allahdadi FA, Sun CT. A quadratic yield function for fiber-reinforced composites. *J Compos Mater* 1999;31:788–811.
- [12] Hill R. A theory of the yielding and plastic flow of anisotropic metals. *Proc R Soc London Ser A* 1948;193:281–97.
- [13] Crisfield MA. *Non-linear finite element analysis of solids and structures*. New York: Wiley; 1997.
- [14] Hou JP, Petrinic N, Ruiz C. Prediction of impact damage in composite plates. *Compos Sci Technol* 2000;60:273–81.
- [15] Clegg RA, Hayhurst CJ. Numerical modelling of the compressive and tensile response of brittle materials under high pressure dynamic loading. *Shock compression of condensed matter*. New York: AIP Press; 1999.
- [16] Thielicke B. Mechanical properties of C/C composites. *Key Eng Mater* 164–165:145–60.